Single objective light-sheet microscopy for high-speed whole-cell 3D super-resolution

Marjolein B. M. Meddens,[1,2] **Sheng Liu,**[1,3] **Patrick S. Finnegan,**[4]
Thayne L. Edwards,[4] **Conrad D. James,**[4] **and Keith A. Lidke**[1,*]

[1] *Department of Physics and Astronomy, University of New Mexico, 1919 Lomas Blvd NE, Albuquerque, NM 87131, USA*
[2] *Department of Pathology, University of New Mexico, 2325 Camino de Salud, Albuquerque, NM 87131, USA*
[3] *Current address: Weldon School of Biomedical Engineering, College of Engineering, Purdue University, West Lafayette, IN 47907, USA*
[4] *Sandia National Laboratories, 1515 Eubank SE, Albuquerque, NM 87123, USA*
[*] *klidke@unm.edu*

Abstract: We have developed a method for performing light-sheet microscopy with a single high numerical aperture lens by integrating reflective side walls into a microfluidic chip. These 45° side walls generate light-sheet illumination by reflecting a vertical light-sheet into the focal plane of the objective. Light-sheet illumination of cells loaded in the channels increases image quality in diffraction limited imaging via reduction of out-of-focus background light. Single molecule super-resolution is also improved by the decreased background resulting in better localization precision and decreased photo-bleaching, leading to more accepted localizations overall and higher quality images. Moreover, 2D and 3D single molecule super-resolution data can be acquired faster by taking advantage of the increased illumination intensities as compared to wide field, in the focused light-sheet.

© 2016 Optical Society of America

OCIS codes: (100.6640) Superresolution; (180.2520) Fluorescence microscopy; (180.6900) Three-dimensional microscopy; (230.3990) Micro-optical devices.

References and links

1. C. S. Smith, N. Joseph, B. Rieger, and K. A. Lidke, "Fast, single-molecule localization that achieves theoretically minimum uncertainty." Nat. Methods **7**, 373–375 (2010).
2. R. J. Ober, S. Ram, and E. S. Ward, "Localization accuracy in single-molecule microscopy." Biophys. J. **86**, 1185–1200 (2004).
3. P. J. Keller and E. H. K. Stelzer, "Digital scanned laser light sheet fluorescence microscopy." Cold Spring Harbor protocols **2010**, pdb.top78 (2010).
4. Y. S. Hu, Q. Zhu, K. Elkins, K. Tse, Y. Li, J. A. J. Fitzpatrick, I. M. Verma, and H. Cang, "Light-sheet Bayesian microscopy enables deep-cell super-resolution imaging of heterochromatin in live human embryonic stem cells," Opt. Nanosc. **2**, 1–12 (2013).
5. J. C. M. Gebhardt, D. M. Suter, R. Roy, Z. W. Zhao, A. R. Chapman, S. Basu, T. Maniatis, and X. S. Xie, "Single-molecule imaging of transcription factor binding to DNA in live mammalian cells." Nat. Methods **10**, 421–426 (2013).
6. F. Greiss, M. Deligiannaki, C. Jung, U. Gaul, and D. Braun, "Single-Molecule Imaging in Living Drosophila Embryos with Reflected Light-Sheet Microscopy," Biophys. J. **110**, 939–946 (2016).
7. T. A. Planchon, L. Gao, D. E. Milkie, M. W. Davidson, J. A. Galbraith, C. G. Galbraith, and E. Betzig, "Rapid three-dimensional isotropic imaging of living cells using Bessel beam plane illumination." Nat. Methods **8**, 417–423 (2011).

#258956 Received 29 Feb 2016; revised 12 Apr 2016; accepted 9 May 2016; published 17 May 2016

8. F. Cella Zanacchi, Z. Lavagnino, M. Perrone Donnorso, A. Del Bue, L. Furia, M. Faretta, and A. Diaspro, “Live-cell 3D super-resolution imaging in thick biological samples.” Nat. Methods **8**, 1047–1049 (2011).
9. B.-C. Chen, W. R. Legant, K. Wang, L. Shao, D. E. Milkie, M. W. Davidson, C. Janetopoulos, X. S. Wu, J. A. Hammer, Z. Liu, B. P. English, Y. Mimori-Kiyosue, D. P. Romero, A. T. Ritter, J. Lippincott-Schwartz, L. Fritz-Laylin, R. D. Mullins, D. M. Mitchell, J. N. Bembenek, A.-C. Reymann, R. Bohme, S. W. Grill, J. T. Wang, G. Seydoux, U. S. Tulu, D. P. Kiehart, and E. Betzig, “Lattice light-sheet microscopy: Imaging molecules to embryos at high spatiotemporal resolution,” Science **346** (2014).
10. C. a. Konopka and S. Y. Bednarek, “Variable-angle epifluorescence microscopy: A new way to look at protein dynamics in the plant cell cortex,” Plant J. **53**, 186–196 (2008).
11. M. Tokunaga, N. Imamoto, and K. Sakata-Sogawa, “Highly inclined thin illumination enables clear single-molecule imaging in cells.” Nat. Methods **5**, 159–161 (2008).
12. R. Galland, G. Grenci, A. Aravind, V. Viasnoff, V. Studer, and J.-B. Sibarita, “3D high- and super-resolution imaging using single-objective SPIM.” Nat. Methods **12**, 641–644 (2015).
13. K. T. Seale, R. S. Reiserer, D. a. Markov, I. a. Ges, C. Wright, C. Janetopoulos, and J. P. Wikswo, “Mirrored pyramidal wells for simultaneous multiple vantage point microscopy.” J. Microsc. **232**, 1–6 (2008).
14. Y. W. Xu, A. Michael, and C. Y. Kwok, “Formation of ultra-smooth 45 micromirror on (100) silicon with low concentration TMAH and surfactant: Techniques for enlarging the truly 45 portion,” Sens. Actuators, A **166**, 164–171 (2011).
15. K. P. Rola, K. Ptasiński, A. Zakrzewski, and I. Zubel, “Silicon 45 micromirrors fabricated by etching in alkaline solutions with organic additives,” Microsyst. Technol. **20**, 221–226 (2013).
16. C. C. Valley, S. Liu, D. S. Lidke, and K. A. Lidke, “Sequential Superresolution Imaging of Multiple Targets Using a Single Fluorophore,” PLoS One **10**, e0123941 (2015).
17. J. Schindelin, I. Arganda-Carreras, E. Frise, V. Kaynig, M. Longair, T. Pietzsch, S. Preibisch, C. Rueden, S. Saalfeld, B. Schmid, J. Y. Tinevez, D. J. White, V. Hartenstein, K. Eliceiri, P. Tomancak, and A. Cardona, “Fiji: an open-source platform for biological-image analysis,” Nat. Methods **9**, 676–682 (2012).
18. G. T. Dempsey, J. C. Vaughan, K. H. Chen, M. Bates, and X. Zhuang, “Evaluation of fluorophores for optimal performance in localization-based super-resolution imaging,” Nat. Methods **8**, 1027–1036 (2011).
19. F. Huang, T. M. P. Hartwich, F. E. Rivera-Molina, Y. Lin, W. C. Duim, J. J. Long, P. D. Uchil, J. R. Myers, M. A. Baird, W. Mothes, M. W. Davidson, D. Toomre, and J. Bewersdorf, “Video-rate nanoscopy using sCMOS camera-specific single-molecule localization algorithms.” Nat. Methods **10**, 653–658 (2013).
20. F. Huang, S. L. Schwartz, J. M. Byars, and K. A. Lidke, “Simultaneous multiple-emitter fitting for single molecule super-resolution imaging.” Biomed. Opt. Express **2**, 1377–1393 (2011).
21. G. W. Zack, W. E. Rogers, and S. A. Latt, “Automatic measurement of sister chromatid exchange frequency.” J. Histochem. Cytochem. **25**, 741–753 (1977).
22. S. Liu, E. B. Kromann, W. D. Krueger, J. Bewersdorf, and K. A. Lidke, “Three dimensional single molecule localization using a phase retrieved pupil function.” Opt. Express **21**, 29462–29487 (2013).
23. Y. Lin, J. J. Long, F. Huang, W. C. Duim, S. Kirschbaum, Y. Zhang, L. K. Schroeder, A. A. Rebane, M. G. M. Velasco, A. Virrueta, D. W. Moonan, J. Jiao, S. Y. Hernandez, Y. Zhang, and J. Bewersdorf, “Quantifying and optimizing single-molecule switching nanoscopy at high speeds.” PLoS One **10**, e0128135 (2015).
24. M. G. L. Gustafsson, L. Shao, P. M. Carlton, C. J. R. Wang, I. N. Golubovskaya, W. Z. Cande, D. A. Agard, and J. W. Sedat, “Three-dimensional resolution doubling in wide-field fluorescence microscopy by structured illumination.” Biophys. J. **94**, 4957–4970 (2008).

---

1. Introduction

Single molecule super-resolution (SMSR) imaging is performed by localizing individual fluorophores within a densely labeled sample. SMSR in 3D throughout a mammalian cell is difficult because wide field activation and imaging light cannot be targeted to the in-focus image plane. This results in high background fluorescence leading to large localization errors [1,2]. To prevent high background fluorescence in SMSR imaging total internal reflection fluorescence (TIRF) illumination is often used to confine the excitation light to ≈300 nm above the coverslip, but this limits the application to imaging of targets close to the ventral plasma membrane. To overcome these limitations, we use a single objective along with a reflective surface to generate illumination only in the image focal plane. We will refer to this method as Single Objective Light-Sheet Microscopy (SO-LSM).

In traditional light-sheet microscopy (also termed selective/single plane illumination microscopy, SPIM) an objective placed perpendicular to the detection objective is used to generate a thin sheet of light that illuminates only the image focal plane [3]. This optical design

#258956 Received 29 Feb 2016; revised 12 Apr 2016; accepted 9 May 2016; published 17 May 2016

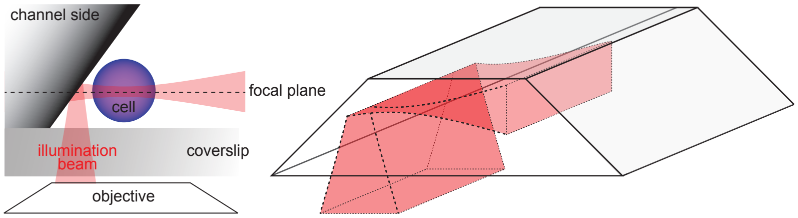

Fig. 1. Principle of reflected beam light-sheet microscopy. A laser line is focused through the objective and is reflected from a 45° mirror side wall of a microfluidic channel. The light-sheet is reflected at the focal plane of the objective, thereby illuminating only the in-focus plane of the cell. 3D optical sectioning is achieved by moving the channel and cell up and downwards and repositioning of the light-sheet such that it is reflected at the focal plane.

requires a specialized microscope in which the illumination and detection objectives have to be placed close together. When high numerical aperture (NA) objectives are needed as is the case for SMSR imaging, this two objective design poses problems due to the short working distance and bulky nature of these objectives. Various attempts have been made to circumvent these limitations. Hu and coworkers proposed a method termed light-sheet Bayesian super-resolution in which they use a prism-coupled condenser design to illuminate a thin slice [4]. In reflected light-sheet microscopy two opposing objectives are used together with a polished AFM cantilever which reflect the light-sheet formed by one objective at the focal plane of the other objective [5]. Recently, this approach was adapted to use commercially available micro-prisms attached to standard coverslips instead of the AFM cantilever [6]. Other approaches include Bessel beam plane illumination [7], individual molecule localization–selective plane illumination microscopy [8] and lattice light-sheet microscopy [9]. However, all these setups are complex and require two objectives that need to be critically aligned, which limits the applicability. Highly inclined and laminated optical sheet (HILO) (also termed variable-angle epi-fluorescence microscopy) uses only one objective, but the field of view is limited by the oblique illumination and the illumination intensity varies with z–depth [10, 11]. Recently, Galland and coworkers used a single objective combined with a 45° reflective surface to produce SPIM 3D optical sectioning and termed their method single-objective selective-plane illumination microscopy (soSPIM) [12].

Here, we describe the use of a single objective, inverted epi-fluorescence microscope along with a reflective surface for illumination and detection (Fig. 1), related to the approach taken by Galland et al. [12]. In our approach the reflective surface forms the side wall of a microfluidic channel incorporated into a microfluidic device. A light-sheet is generated through the objective and reflected by the mirror surface such that it illuminates only the in-focus plane of the cell (Fig. 1). The microfluidic device provides benefits such as a sealed environment and fast, automated buffer exchange which are beneficial for SMSR applications where buffer conditions are critical.

2. Optical design

2.1. Layout of optical setup

The outline of the optical setup is shown in Fig. 2. The microscope's excitation source is a 642 nm diode laser (Thorlabs, HL6366DG) which is collimated by aspherical lens AL1 and a laser diode clean up filter is used to filter out undesirable laser light (Semrock, LD01-640/8-12.5). The laser is coupled into an optical fiber (P1-488PM-FC-2, 0.12 NA, Thorlabs) via two

#258956 Received 29 Feb 2016; revised 12 Apr 2016; accepted 9 May 2016; published 17 May 2016

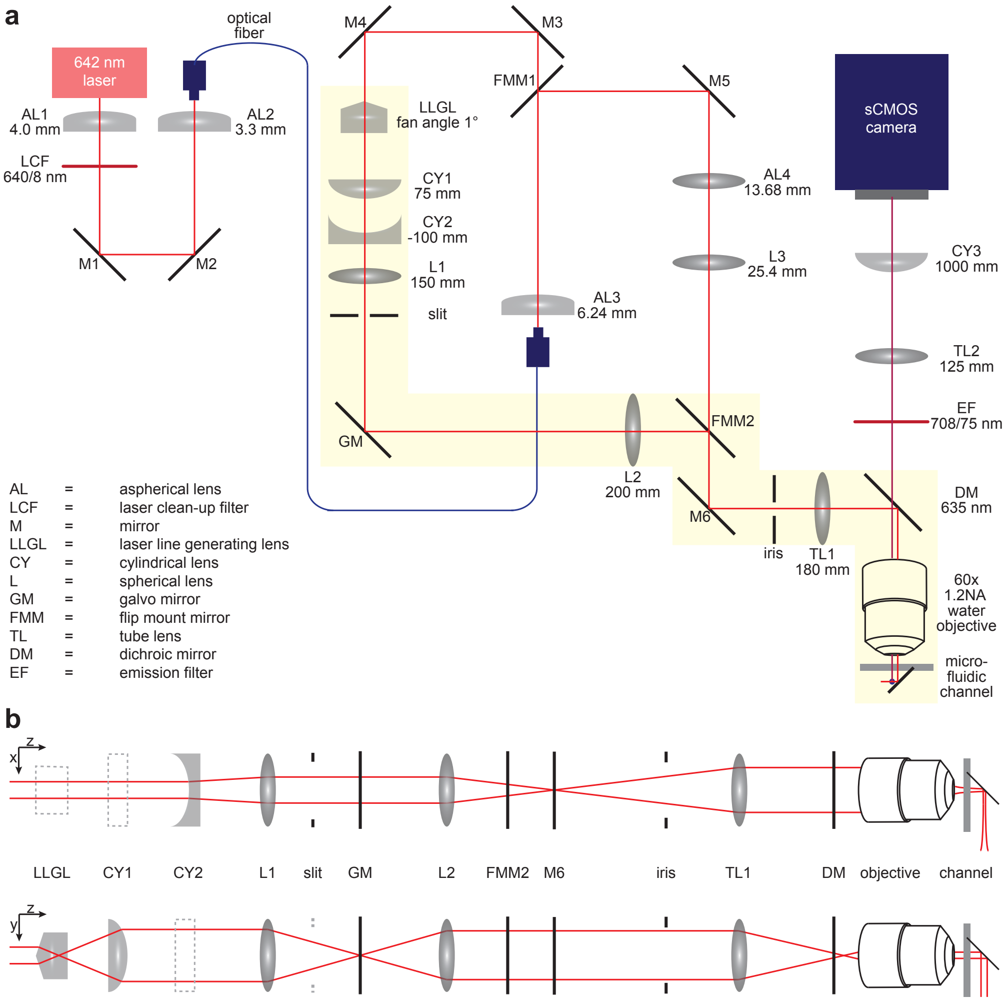
a
642 nm laser
optical fiber
AL1 4.0 mm
AL2 3.3 mm
LCF 640/8 nm
M1
M2
M4
M3
FMM1
M5
LLGL fan angle 1°
CY1 75 mm
CY2 -100 mm
L1 150 mm
slit
AL3 6.24 mm
AL4 13.68 mm
L3 25.4 mm
sCMOS camera
CY3 1000 mm
TL2 125 mm
EF 708/75 nm
GM
L2 200 mm
FMM2
M6
iris
TL1 180 mm
DM 635 nm
60x 1.2NA water objective
micro-fluidic channel
AL = aspherical lens
LCF = laser clean-up filter
M = mirror
LLGL = laser line generating lens
CY = cylindrical lens
L = spherical lens
GM = galvo mirror
FMM = flip mount mirror
TL = tube lens
DM = dichroic mirror
EF = emission filter
b
z
x
LLGL
CY1
CY2
L1
slit
GM
L2
FMM2
M6
iris
TL1
DM
objective
channel
z
y

Fig. 2. Single objective light-sheet microscope setup. (a) Schematic overview of microscope setup. The image shows the horizontal plane of the optical table. Note that the objective and microfluidic channel are drawn horizontally for visualization purposes, but they actually point upwards. (b) The laser line generating light paths (yellow highlighted part in (a) are shown for the *x*–*z* and *y*–*z* planes.

#258956 Received 29 Feb 2016; revised 12 Apr 2016; accepted 9 May 2016; published 17 May 2016

mirrors and aspherical lens AL2. The laser beam out of the fiber is collimated by an aspherical lens, AL3. For the wide field illumination light path, flip mount mirror FMM1 is flipped up and reflects the light onto mirror M5. The laser beam passes through a telescope system formed by aspherical lens AL4 and lens L3, which expand the beam into the desirable diameter. Flip mount mirror FMM2 is flipped down and mirror M6 reflects the light through the iris and TL1 onto the dichroic mirror (Semrock, Di02-R635-25x36) and into the objective (Olympus, UPLSAPO 60X W), which is placed vertically in an inverted microscope configuration. The fluorescence emission passes through the dichroic mirror DM and an emission filter EM (Semrock, FF01-708/75-25) before being focused by tube lens TL2 onto an sCMOS camera (Hamamatsu ORCA-Flash4.0 V2 Digital CMOS, C11440-22CU). A cylindrical lens CY3 is placed 46 mm before the camera chip to create astigmatism for 3D emitter localization. The cylindrical lens CY3 is removed for diffraction limited imaging and 2D super-resolution.

For light-sheet generation, flip mount mirror FMM1 is flipped down and the laser is reflected by mirrors M3 and M4. Figure 2(b) shows the light paths for the x–z and y–z plane with z being the dimension along the optical axis. In the x–z plane, the laser line is diverged by a cylindrical lens, CY2, and re-collimated by lens L1. When the beam is collimated after L1 the waist of the light-sheet will be positioned at the focal plane of the objective, however this is not the ideal position as it will diverge right after reflection by the channel wall, before reaching the cell. Therefore the position of CY2 is not fixed and can be adjusted along the optical axis to position the beam waist further away from the focal plane of the objective and within the cell after reflection (see section 2.2). A slit is used to control the x dimension of the laser line. After reflection by the galvanometric mirror GM, and the flip mount mirror FMM2, which is flipped up for light-sheet illumination, the laser line is focused in the x–z plane at mirror M6. Mirror M6 is placed at the conjugate focal plane of the sample plane, which is 180 mm from the tube lens, TL1. Therefore, the focused laser line at the M6 will be imaged at the sample plane through the tube lens TL1, the dichroic mirror DM, and the objective. In the y–z plane, the laser beam is expanded by the laser line generating lens LLLG (LaserLine Optics Canada, LOCP-8.9R01-1.0), and re-collimated by a cylindrical lens CY1. L1 focuses the laser in the y–z plane at the galvanometric mirror GM. After being reflected by the galvanometric mirror, the laser line is diverging in y–dimension, and is collimated by L2. After reflection by flip mount mirror FMM2, mirror M6 and passing through the iris the laser line is imaged by tube lens TL1 and the objective. The laser line is reflected by the side wall of a microfluidic channel and forms a light-sheet in x–y, across the focal plane of the objective.

The sample is placed in a sample holder (Thorlabs, MAX3SLH) which is mounted onto x and y manual translational stages (Thorlabs, PT1/M). The sample z–position is controlled by a combined manual/piezo translational stage (Thorlabs, NFL5DP20S/M). The piezo is coupled to a strain gauge reader for feedback and operated in closed loop control. For z–scanning the piezo is used to scan the sample in z and the galvanometric mirror is used to position the light-sheet at the correct x–position such that it is reflected at the focal plane of the objective.

2.2. *Positioning the beam waist at the cell*

In the ideal situation, the entire length of the light sheet (confocal parameter) should be centered on the cell, so that the thinnest part of the light-sheet spans across the cell area. Therefore, the beam waist should be moved further away from the objective. To achieve this, the incoming beam should not be collimated and the beam curvature at the back aperture of objective lens should not be infinite, but should have a finite value. In Fig. 3, R_1 is the beam curvature at the back aperture of the objective. Given that R_1 is approximately tens of millimeters large it can be approximated to the object distance of the intermediate virtual object of the beam waist inside the sample medium. In order to move the beam waist away from the objective, the best option

#258956 Received 29 Feb 2016; revised 12 Apr 2016; accepted 9 May 2016; published 17 May 2016

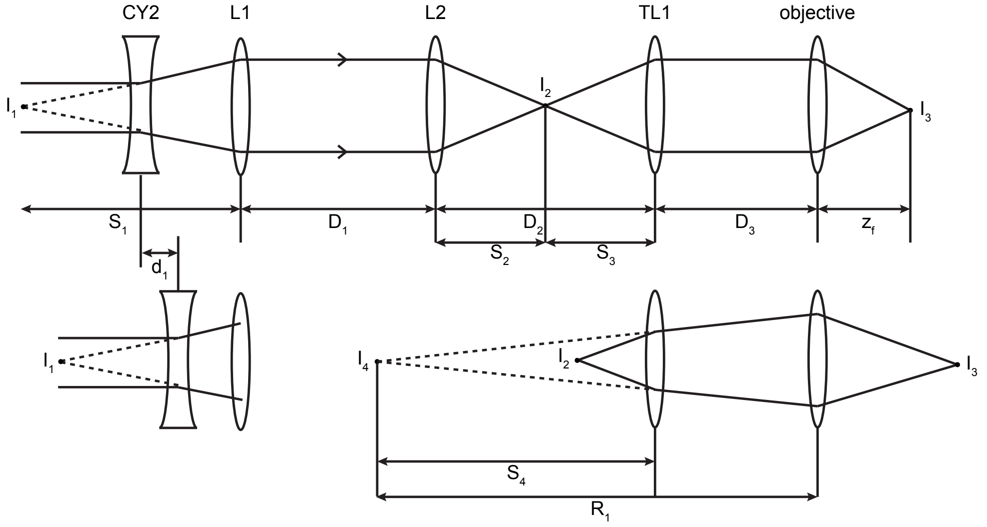

Fig. 3. Positioning the beam waist. The beam path in the x–z dimension is shown starting from CY2 (top). The optical components are labeled the same as in Fig. 2. I_1 is the virtual object of I_2, I_2 is the real object of I_3, which is the beam waist, and I_4 is both the virtual image of I_2 and the virtual object of I_3. If I_3 is at the designed focal position of the objective lens, S_1 is equal to the focal length of $L_1 (S_1 = f_1)$. D_1, D_2 and D_3 are fixed distances, which are equal to $f_1 + f_2$,$f_2 + f_3$ and f_3, respectively (D_3 is approximately equal to f_3, because the focal length of the objective lens is usually much smaller than the focal length of the tube lens TL1). In the bottom drawing, CY2 is moved by a distance d_1, and thereby the beam waist I_3 is moved away from the objective lens.

is to move the second cylindrical lens (CY2, Fig. 2), which will affect only the optical path in the x–z dimension. Figure 3 shows the excitation beam path in the x–z dimension starting from CY2. As shown in the top panel, if I_3 is at the designed focus of the objective, its virtual object I_4 will be at infinity, and $R_1 \approx \infty$, $S_1 = f_1$, in which f_1 is the focal length of lens L1. By moving CY2 a distance of d_1 (bottom panel), I_4 is moved towards the objective, and R_1 gets a finite value. The derivation of R_1 from d_1 is given below. Lens L1 and L2 form a telescopic system, with an axial magnification of $(f_2/f_1)^2$, in which f_2 is the focal length of L2. Thus S_2, which is originally equal to f_2, can be calculated from

$$S_2 = \left(\frac{f_2}{f_1}\right)^2 \times d_1 + f_2 \tag{1}$$

since D_2 is fixed and equal to $f_2 + f_3$, S_3 is given by:

$$S_3 = f_2 + f_3 - S_2 \tag{2}$$

although TL1 and the objective also form a telescope like system, its lateral magnification does not agree with the result from a telescope system, because the objective is a compound lens system, which cannot be simplified by a thin lens. The image formation of TL1 is described by:

$$\frac{1}{S_3} - \frac{1}{S_4} = \frac{1}{f_3} \tag{3}$$

then:

$$R_1 = S_4 + D_3 = S_4 + f_3 \tag{4}$$

#258956 Received 29 Feb 2016; revised 12 Apr 2016; accepted 9 May 2016; published 17 May 2016

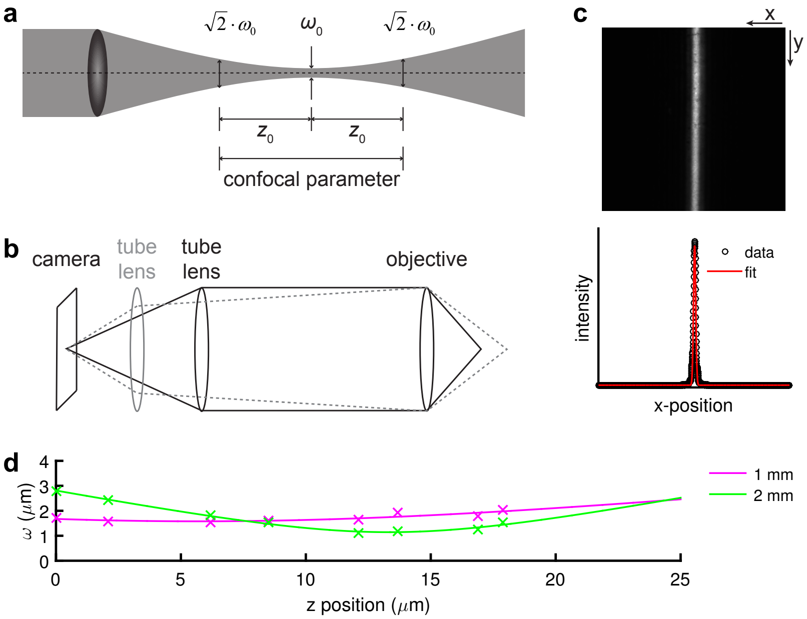

Fig. 4. Light-sheet dimensions. (a) Cartoon representing the measured parameters of the beam dimensions. ω_0 is the beam radius at the waist, z_0 is the distance between the waist and the position along the propagation direction at which the beam radius is $\sqrt{2} \times \omega_0$. The confocal parameter is $2 \times z_0$. (b) In order to image the beam dimension at various distances from the objective the position of the tube lens relative to the camera is changed, resulting in a shift of the focal plane. (c) At each focus an image of the beam is taken (top panel) and the profile of the image along the x dimension is fitted to a Gaussian in order to determine the width. (d) Graph showing the measured beam width (crosses) for each z-position (propagation direction), where 0 is the closest position to the objective that we could measure. The beam was measured for two different slit aperture widths (1 mm and 2 mm) and for both the profile was fit to Eq. (6).

combining Eqs. (1) to (4)

$$R_1 = \left(\frac{f_1 \times f_3}{f_2}\right)^2 \times \frac{1}{d_1} \tag{5}$$

Thus, z_f can be related with d_1 by Eq. (5) and CY2 can be moved towards the objective in order to move the beam waist away from the objective and the channel wall and into the cell.

2.3. *Light-sheet dimensions*

We measured the dimensions of the light-sheet (Fig. 4(a)) by moving the tube lens with respect to the camera and imaging an Alexa 647 coated coverslip (Fig. 4(b,c), see section 4.2 for details). For a 2 mm slit opening, which is approximately the x–dimension of the beam at the slit position, we found the thickness (ω_0) of the light-sheet to be 1.1 µm and the confocal parameter (range over which the thickness is smaller than $\sqrt{2} \times \omega_0$) to be 11.9 µm (Fig. 4(d)), thereby matching the dimensions of a single cell. Increasing the slit opening didn't change the beam profile (data not shown). We can tune the light-sheet dimensions by closing the slit, as is shown for a 1 mm slit opening (Fig. 4(d)), which increases the thickness to 1.6 µm and the confocal parameter to be 32.3 µm. This allows for imaging of larger cells by compromising the light-sheet thickness and intensity. The size of the light-sheet in the y–dimension (width) is 27 µm, which results in a size of the field of view of $11.9 \times 27\,\mu m$ for a 2 mm slit opening and $32.3 \times 27\,\mu m$ for a 1 mm slit opening. To increase the field of view for larger cells the *y*–dimension of the beam could be tuned by changing the fan angle of the laser line generating lens.

3. Microfluidics chip design and fabrication

Microfluidic chips with integrated reflective surfaces were produced using bulk-micromachining of silicon. Several methods currently exist to fabricate and optimize 45° angled sidewalls in silicon [13, 14], and for this effort we have utilized the potassium hydroxide (KOH) with organic surfactant approach [15]. The schematic of the device fabrication approach is shown in Fig. 5(a). Silicon wafers with (1 0 0) orientation were cleaned and then a 1 µm thermal oxide layer was grown on the substrates. Photoresist was spun on wafers, and channel features of varying width (50 µm to 300 µm) were created on the substrates using photolithography. The features were then transferred into the oxide with a reactive ion etch. Channels with 45° angled sidewalls were then etched into the silicon substrate using a KOH solution with TritonX-100 detergent added to improve the smoothness of the etched sidewalls [15]. Since the KOH etch chemistry is selective for silicon and does not etch the silicon dioxide, the oxide mask is undercut during the etch process leaving oxide overhangs (Fig. 5(a(iv),c)). After the wet etch process, the substrates were rinsed thoroughly, and subjected to a buffered hydrofluoric acid (HF) etch to remove the oxide mask. Using a contact profilometer, the sidewall angle for etched microchannels was determined to be $42.9 \pm 0.63°$ for a microchannel depth of $41.3 \pm 1.7\,\mu m$ (n=20). As expected from an anisotropic etch determined by the silicon crystal orientation, SEM imaging indicated that the microchannel sidewalls were qualitatively flat over the length of the sidewall with some curvature at the crystal plane intersections at the top and bottom of the channels (Fig. 5(d)). Atomic force microscopy (AFM) was used to examine the surface roughness of the sidewalls ($R_{rms} = 4.14\,\text{nm}$) in comparison to the roughness of the top of the silicon wafer that was previously under the oxide mask ($R_{rms} = 1.75\,\text{nm}$). The top surface of the channel has increased surface roughness due to the difference in the etching plane of the bottom surface (1 0 0) to the sidewalls (1 1 0). After another batch of thorough rinsing, substrates were placed into an evaporator and coated with a thin layer of aluminum metal. Aluminum was chosen due to its high reflectivity in the optical wavelength range compared to other metals. Figure 5(d) shows a channel with 45° angled sidewalls as measured with scanning electron microscopy (SEM) and contact profilometry. After wafers were coated with aluminum, they were sawed into chips and anodically-bonded to pyrex coverslips to enclose the microchannels.

To create a reliable fluidic and optical interface with the microfluidic chip it was housed in a plastic laminate package. The package was made from five layers of adhesive coated and uncoated plastic sheets (Fig. 6(a)). Each sheet was laser cut and then laminated together to form a three dimensional mechanical housing to which the microfluidic chip was attached (Fig. 6(b)). The upper four layers were comprised of 2.0 mm polymethylmethacrylate (PMMA, Astra Products), 0.10 mm acrylic adhesive tape (90445, Adhesives Research), 2.0 mm PMMA, and 0.10 mm 90445 tape. These layers house silicon O–rings (dash 001, McMaster-Carr) which received and supported PEEK or PTFE tubing (OD, $1/32$ inch) used to supply buffers, gel, sample, and cleaning reagents to each of the channels individually. The lower three layers were comprised of 0.5 mm PMMA (Astra Products), 0.10 mm 90445 tape, and 0.20 mm PMMA (Astra Products). The functionality of the PMMA layers was mechanical support and alignment of the microfluidic chip. The tape layer provided a channel for the gel to be loaded in the mirrored micro-channel without interfering with subsequent introductions of fluids (Fig. 6(c)). The bottom side of the adhesive was also used to adhere the microfluidic chip (silicon side) to the package. The final arrangement of the package resulted in the imaging-side of the microfluidic chip oriented opposite of the fluidic tubing interface (Fig. 6(d,e)), which package was then

#258956 Received 29 Feb 2016; revised 12 Apr 2016; accepted 9 May 2016; published 17 May 2016

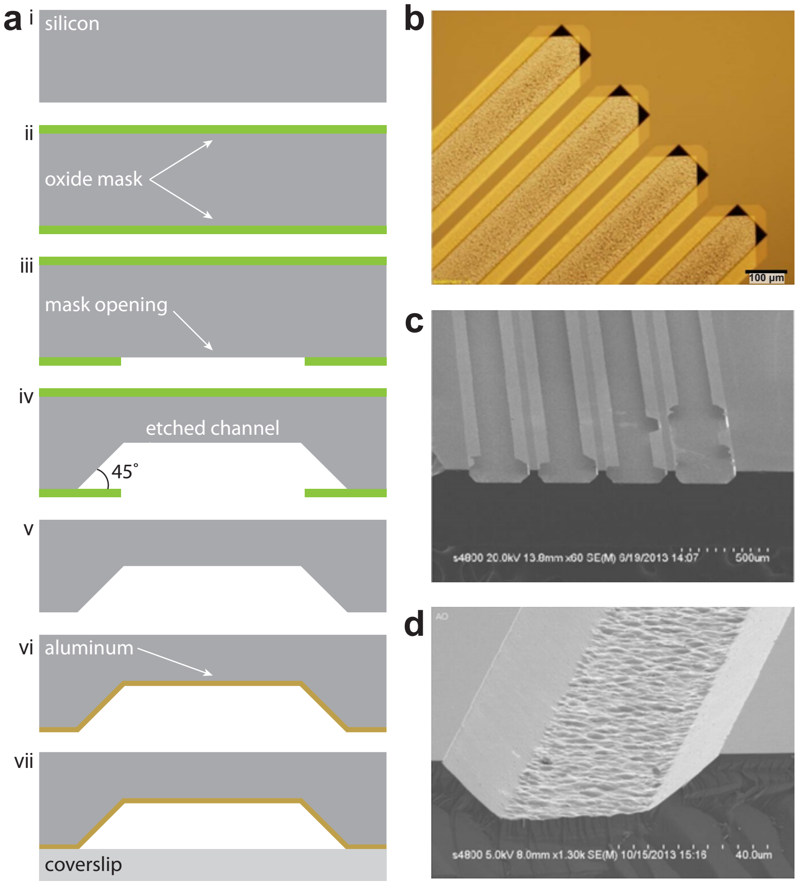
a
i
silicon
ii
oxide mask
iii
mask opening
iv
etched channel
45°
v
vi
aluminum
vii
coverslip
b
100 µm
c
s4800 20.0kV 13.8mm x60 SE(M) 6/19/2013 14:07
500um
d
s4800 5.0kV 8.0mm x1.30k SE(M) 10/15/2013 15:16
40.0um

Fig. 5. Channel fabrication and characterization. (a) Schematic of channel fabrication. A silicon wafer is used to etch the channel (i). An oxide mask is grown on the silicon (ii) and a mask opening is created by photolithography (iii). The channel is etched by KOH which leaves oxide mask overhangs (iv). The mask is removed (v) and the channel surface is coated with aluminum (vi) before being anodically bonded to a glass coverslip (vii). (b) Optical microscope image of four channels. (c) SEM image of four channels after KOH etch but before HF etch showing oxide mask overhangs. (d) SEM image depicting a single channel after HF etch to remove oxide mask.

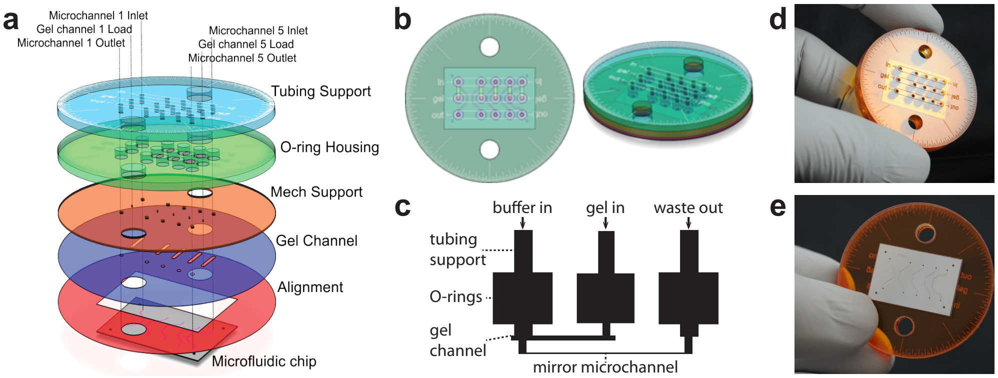
a
Microchannel 1 Inlet
Gel channel 1 Load
Microchannel 1 Outlet
Microchannel 5 Inlet
Gel channel 5 Load
Microchannel 5 Outlet
Tubing Support
O-ring Housing
Mech Support
Gel Channel
Alignment
Microfluidic chip
b
c
buffer in
gel in
waste out
tubing support
O-rings
gel channel
mirror microchannel
d
e

Fig. 6. Chip layout. (a) Exploded view of chip packaging. Each chip is packaged into five layers of PMMA with two O-rings incorporated for each in and outlet. (b) Transparent top and side view images of chip assembled in packaging. (c) Schematic showing the fluidic connections inside the chip. (d,e) Photographs showing top (d) with tubing connections and bottom (e) with coverslip surface of packaged chip.

secured into the microscope setup.

4. Materials and methods

4.1. *Characterization of microfluidic channels with* 45° *mirror side walls*

SEM was performed to image the channels after fabrication, using a Hitachi S4800 microscope. AFM was performed to characterize the surface roughness of the reflective surfaces. A Dimension 5000 microscope was used in tapping mode, and the raw data was modified by leveling to order 1.

4.2. *Measurement of light-sheet dimensions*

The profile of a focused Gaussian beam along the optical axis is described by:

$$\omega_z = \sqrt{\omega_0 \times \left(1+\left(\frac{z}{z_0}\right)^2\right)} \tag{6}$$

where ω_z is the beam radius at which the field intensity drops to $1/e^2$ of the axial value, ω_0 is the beam radius at position z_0 which is the minimum value of ω_z and known as the beam waist (Fig. 4(a)). To measure the dimensions of the light-sheet coming out of the objective an 8-well chamber slide (LabTek) was coated with AlexaFluor 647 and positioned above the objective. In order to image multiple focal planes above the objective without changing the light-sheet, the tube lens was moved to and from the camera (Fig. 4(b)). For each position of the tube lens the piezo stage was used to move the fluorescent slide into the focal plane and 100 images of the beam profile illuminating the slide were recorded for 3 slit apertures. The z–position of the piezo was recorded with the images and the position of the tube lens was marked. Next, the tube lens was moved to another position and the procedure was repeated. After images were acquired for each position of the tube lens, the fluorescent slide was exchanged for a calibration grid with known dimensions (Thorlabs, R1L3S3P). For each position of the tube lens the grid was imaged to determine the magnification of the system with the tube lens at that position. The y-projection of the mean of the 100 images was corrected for the measured magnification and fitted to a Gaussian function to determine the beam width (Fig. 4(c)). Next, the beam width was plotted against the z–position (as recorded by the piezo) for each slit aperture width and the resulting curves were fitted to Eq. (6) (Fig. 4(d)).

4.3. *Cell lines and reagents*

HeLa cells were cultured in Dulbeccos Modified Eagle Medium (Life Technologies # 10313-021) supplemented with 10 % fetal bovine serum (HyClone), penicillin-streptomycin, and 2 mM L-glutamine at 37 °C and 5 % CO_2. RBL-2H3 cells were cultured in MEM (Life Technologies #11095-080) supplemented with 10 % fetal bovine serum (HyClone) penicillin-streptomycin, and 2 mM L-glutamine at 37 °C and 5 % CO_2. Mitochondria were labeled with 5 µg mL^{-1} anti-TOM20 antibody (Santa Cruz Biotechnology, sc-11415) which was conjugated to AlexaFluor647 carboxylic acid, succinimidyl ester (A-20006, Life Technologies) as described earlier [16].

4.4. *Fixation and labeling*

All labeling and washing steps were carried out at room temperature while rotating unless stated otherwise. Cells were harvested by trypsin and suspension cells were fixed in 4 % paraformaldehyde in PBS for 2 h. Cells were washed once with PBS and were blocked and permeabilized in PBS + 5 % BSA + 0.05 % Triton X-100 for 15 min to 30 min and stored at 4 °C in PBS + 2 % BSA + 0.05 % NaN_3. Cells were labeled with primary antibody in PBS + 2 % BSA + 0.05 % Triton X-100 for 2 h at room temperature followed by extensive washing in PBS + 2 % BSA.

4.5. *Diffraction limited imaging*

For diffraction limited imaging, fixed and labeled cells were loaded into Poly-L-lysine (PLL) coated channels in PBS by a syringe pump and were left to settle for 1 h before the PBS was replaced by imaging buffer. Imaging was performed in an imaging buffer with enzymatic oxygen scavenging system: 50 mM Tris, 10 mM NaCl, 10 % w/v glucose, 168.8 U mL^{-1} glucose oxidase (Sigma #G2133), 1404 U mL^{-1} catalase (Sigma #C9332). Diffraction limited images were acquired by taking 15 frames at each z–plane, with planes being 250 nm apart. The exposure time was 20 ms frame^{-1}. In Fig. 7 images are the background corrected mean of all images taken at one z–plane. Line profiles and orthogonal projections were calculated from these mean images using Fiji [17].

4.6. *SM–SR imaging*

Cells were imaged in standard dSTORM imaging buffer [18] with enzymatic oxygen scavenging system supplemented with 50 mM 2-aminoethanethiol (MEA), pH 8.5. For SMSR imaging suspension cells were imaged in a 1 % low melting temperature agarose (A9045, Sigma Aldrich) gel. The gel was prepared by dissolving agarose in PBS using microwave heating. Aliquots of 4 % agarose solutions were stored at 4 °C until use. Agarose aliquots were heated to 80 °C to melt and cooled to 37 °C before mixing with cells. Cells were washed once in dSTORM buffer before mixing with the agarose. The agarose-cell mixture was diluted in dSTORM buffer to get a 1 % agarose concentration. Before cell loading the microfluidic chip was filled with dSTORM buffer through the buffer inlet. The agarose-cell mixture was loaded through the gel inlet port using a manual syringe while the channel was imaged close to the outlet port to assure the whole channel was filled. Next, the channel was cooled on ice for 5 min to let the agarose gel. The chip was assembled on the microscope stage and left to equilibrate to room temperature for 15 min before perfusion of dSTORM buffer was started and imaging was performed. dSTORM buffer was flown through the gel at 10 nL min^{-1} during image acquisition.

For wide field illumination, cells were not imaged in the microfluidic chips because reflections from the mirror walls and top of the channel created high background. Instead cells were

#258956 Received 29 Feb 2016; revised 12 Apr 2016; accepted 9 May 2016; published 17 May 2016

imaged in an 8-well chamber. To mimic the imaging conditions in the channel the cells were also imaged in a 1 % agarose gel.

For 2D SMSR imaging a single plane was imaged for 200 sequences of 2000 frames. For 3D whole-cell imaging cells were imaged from bottom to top, 2000 frames were acquired at each z-plane and planes were spaced 250 nm apart. The scan was repeated throughout the whole-cell twelve times resulting in 24 000 frames for each z–position. For wide field and light-sheet illumination the acquisition procedure was the same.

4.7. *Super-resolution image analysis and reconstruction*

For both 2D and 3D super-resolution raw data were converted to photon counts by subtracting a pixel specific offset and multiplying by a pixel specific gain factor as described for sCMOS cameras [19]. We accounted for the pixel dependent read noise in our fitting algorithms as described earlier [19].

For 2D super-resolution imaging single emitters in each frame are identified as described [20]. The method performs two filtering steps to reduce the Poisson noise and smooth out the data, then finds the pixel coordinates of local maxima and uses these as the centers of fitting regions. Each fitting region measured 7 × 7 pixels and all fitting regions were fed into the 2D localization algorithm that maximize the likelihood function using a Newton-Raphson method to iteratively update the fitting parameters, which includes the x and y positions, the total photon count, the background photon counts and the size (σ) of the PSF. The localized emitters were filtered through thresholds on localization precision calculated from the Cramer-Rao Lower Bound (CRLB) and the p-value. The accepted emitters were used to reconstruct the SR image. Each emitter is represented by a 2D-Gaussian with (σ_x) and (σ_y) equal to the smallest of the localization precision in x and y.

For 3D whole-cell imaging we used a scale space filtering approach to reduce noise and enhance individual emitter signal. The scale space consists of five difference of Gaussians filters with varying x and y dimensions to match in and out of focus shapes of individual emitters. Pixel coordinates of local maxima in the scale space are intensity thresholded using an automated threshold selection method [21] and are used as centers of fitting regions. The fitting region size is 8 × 8 pixels (1.22 µm) and a phase retrieved PSF model is used in a 3D localization algorithm based on maximum likelihood estimation (MLE) [1,22] using a Poisson noise model. All the fitting regions were fed into the 3D localization algorithm that maximizes the likelihood function using a Newton-Raphson method to iteratively update the fitting parameters, which includes the x, y and z positions, intensity, and background photon counts. The localized emitters were filtered by thresholding the intensity, background, p-value and CRLB on σ_x, σ_y and σ_z of the estimate. Localizations were frame connected as described earlier [22]. The accepted emitters were used to reconstruct SR images in which every emitter was plotted as a 3D Gaussian blob with σ_x and σ_y equal to the minimum of the two localization precisions based on the CRLB. The cylindrical lens which is used to create astigmatism of the PSF also alters the magnification in the y–dimension. This results in different pixel sizes in the x and y–dimension, for which we corrected in the image reconstructions.

4.8. *Computation*

All data analysis was performed in Matlab (version 2014a and version 2015a, The Mathworks) with the DIPimage toolbox (http://www.diplib.org/) unless stated otherwise. Position estimation was performed using c-language and NVIDIA CUDA that were compiled to Matlab Mex files [22].

#258956 Received 29 Feb 2016; revised 12 Apr 2016; accepted 9 May 2016; published 17 May 2016

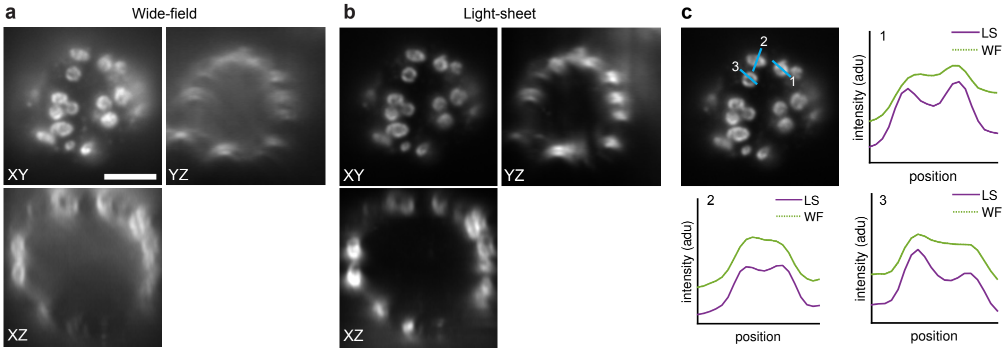

Fig. 7. Light-sheet illumination reduces background and increases contrast in diffraction limited imaging. Images of an RBL cell illuminated in wide field (a) and light-sheet (b) mode. Shown are one x–y plane and x–z and y–z projections. (c) Intensity profiles for the lines shown in (a). Scale bar is 5 µm.

5. Results

To demonstrate the decrease in fluorescence background of single cells we imaged fixed RBL cells labeled for TOM-20 in the microfluidic channels with wide field and light-sheet illumination (Fig. 7(a,b)). Direct comparison of the same cell imaged with wide field and light-sheet illumination clearly demonstrated the reduced background and increased contrast of the mitochondria, highlighted by the intensity profiles through individual mitochondria (Fig. 7(c)).

To investigate the advantages of light-sheet illumination on SMSR imaging we performed 2D dSTORM imaging of mitochondria in HeLa cells. We compared wide field and light-sheet illumination. The 45° mirror surfaces don't extend into the coverslip, therefore the reflection of the light-sheet is not optimal at the first few µm above the coverslip. To prevent the cells from touching the coverslip we imaged them in agarose gel. For wide field illumination we chose to image cells in 8-well chamber dishes in a 1 % agarose gel to prevent increasing the background due to reflections of the chip side walls and top. Figure 8(a,b) shows single cell images obtained with wide field (a) and light-sheet (b) illumination. With wide-field illumination detection and localization of individual emitters is difficult in fluorophore-dense areas of the cell due to illumination of out-of-focus emitters. This results in poorer reconstruction of mitochondrial structure. Moreover, since the light-sheet focuses the illumination in one dimension the illumination intensity is increased. Higher illumination intensities lead to faster blinking kinetics [19, 23], therefore we could image 2.5 times faster with light-sheet than with wide field illumination (2 ms frame^{-1} vs 5 ms frame^{-1}) without decreasing the number of photons per emitter (Fig. 8(c)). The total acquisition times for these images consisting of 150 sequences of 2000 frames were 35 min for wide field illumination and 16 min for light-sheet illumination. Also, quantification of the number of background photons per pixel clearly demonstrates a reduction in background for light-sheet illumination (Fig. 8(d)). This is also reflected in the SNR which is higher for light-sheet than wide field illumination (Fig. 8(e)). This results in a better localization precision, reported as the CRLB on σ_x in Fig. 8(f), is better for light-sheet than for wide field illumination.

To use the SO-LSM setup for whole-cell 3D dSTORM imaging we placed a cylindrical lens in the emission light path to localize individual emitters in 3D. We imaged HeLa cells that were fixed in suspension and immunostained for TOM-20 in the microfluidic chips with light-sheet illumination (2 ms frame^{-1}) and in 8-well chambers with wide field illumination (5 ms frame^{-1}) as described for 2D SMSR. Raw image frames (Fig. 9(a,b)) clearly demonstrate

#258956 Received 29 Feb 2016; revised 12 Apr 2016; accepted 9 May 2016; published 17 May 2016

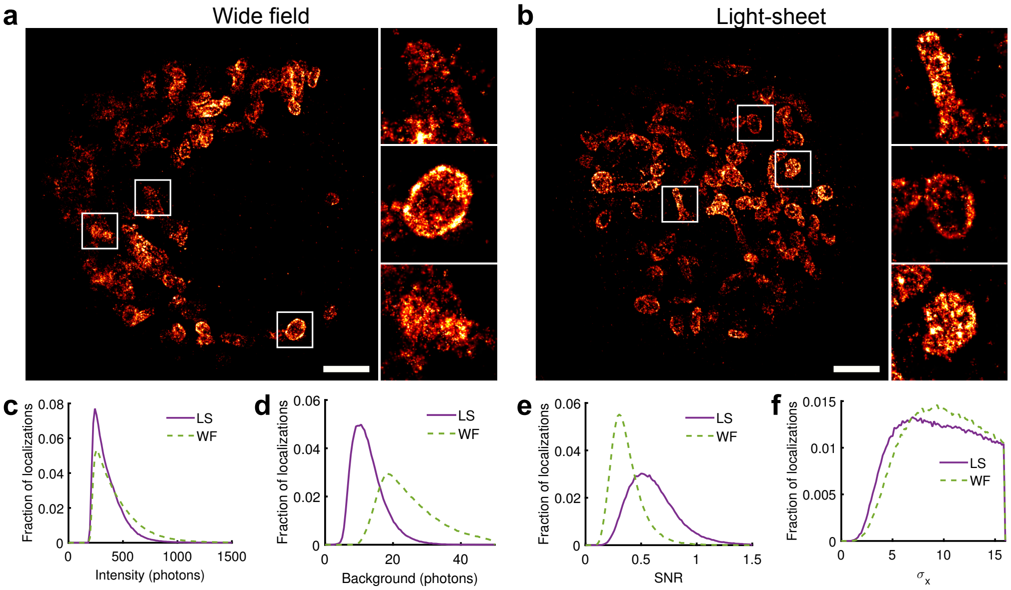

Fig. 8. SO-LSM improves 2D super-resolution microscopy. HeLa cells were labeled for TOM-20 to visualize mitochondria and imaged for 200 sequences of 2000 frames each. 2D reconstructions are shown for cells imaged using wide field (a) and light-sheet illumination (b). White boxes show the position of zoomed in regions shown to the right of each image. Histograms of intensity (c), per pixel background (d), signal to noise ratio (SNR, e) and localization accuracy reported by the CRLB σ_x (f) of individual emitters are shown. Green dotted lines depict results for cells imaged with wide field illumination and solid purple lines depict results for light-sheet illumination. Histograms are summed over 4 cells imaged for each condition. LS = light-sheet, WF = wide field, scale bar 2 µm.

a higher background signal for wide field vs light-sheet illumination. Quantification of single emitter statistics shows that while the number of collected photons (Fig. 9(c)) is the same, the per pixel background (Fig. 9(d)) is reduced for light-sheet illumination. This results in a better SNR (Fig. 9(e)) and a slightly improved localization accuracy (Fig. 9(f)) for the z–position of individual emitters.

There could be several reasons why the difference in SNR doesn't result in an large improvement of the localization accuracy. First, the reported localization accuracy is reported only for accepted emitters. Thresholding of emitters is done based on intensity, background, localization accuracy and p-value of the fit. Therefore, only good localizations will be represented in the plot. Indeed, when we compare all localizations without thresholding and the advantage of light-sheet illumination was more pronounced (data not shown). Moreover, if we compare the acceptance rates of localizations we find that these are higher for light-sheet illumination than for wide field (28 % vs. 25 % respectively). Second, the high background in wide field illumination might prevent low intensity emitters from being detected by our box finding method resulting a bias towards better localization accuracies. However, this will results in fewer detected emitters, thereby decreasing final emitter density and image quality. This effect will be stronger in 3D SMSR than in 2D SMSR, because the 3D PSF is larger due to the astigmatism, thereby decreasing the pixel intensities for single emitters, but not for out-of-focus background.

To investigate the advantage of increased intensity in light-sheet illumination we analyzed the data acquired for Fig. 9 for the same acquisition times. 3D reconstructions are shown for

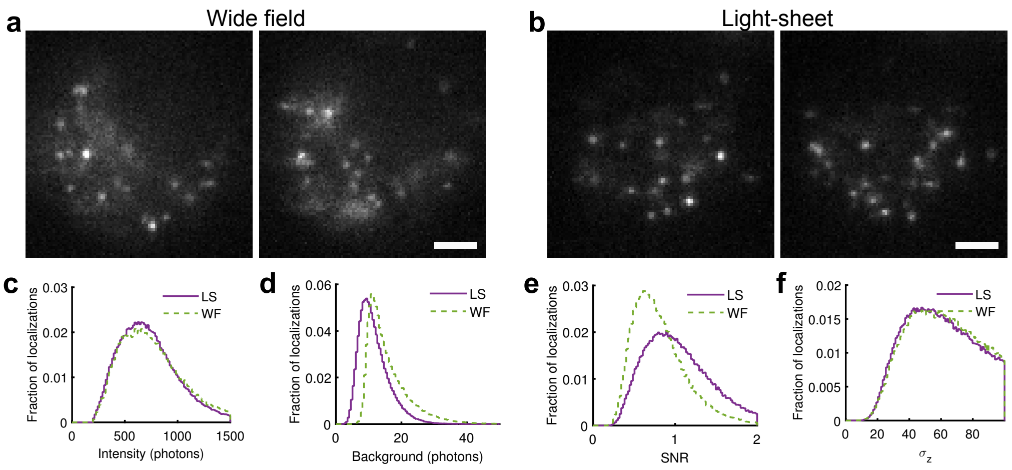

Fig. 9. SO-LSM improves 3D super-resolution microscopy. HeLa cells were labeled for TOM-20 to visualize mitochondria and imaged for 150 sequences of 2000 frames each. Single frame raw data images, corrected for offset and gain, are shown for cells imaged using wide field (a) and light-sheet illumination (b). Histograms of intensity (c), per pixel background (d), signal to noise ratio (SNR, e) and localization accuracy reported by the CRLB on σ_z (f) of individual emitters are shown. Green dotted lines depict results for cells imaged with wide field illumination and solid purple lines depict results for light-sheet illumination. LS = light-sheet, WF = wide field, scale bar 3 µm.

data acquired in 1, 3 and 5 minutes (Fig. 10). For all three time points the images demonstrate better reconstructions for light-sheet than for wide field illumination. After 1 minute the light-sheet image already shows well defined mitochondria whereas hardly anything is visible with wide field illumination. After 3 and 5 minutes mitochondrial membranes are better defined for light-sheet than for wide field illumination. This clearly demonstrates the advantage of higher illumination intensities by light-sheet illumination in decreasing the acquisition time needed for good reconstructed images.

Next, we used imaged complete, top-to-bottom TOM-20 labeled HeLa cells with widefield and light-sheet generation. Figure 11(a,b) shows *x*–*y* whole-cell projections of the reconstructed images which are color-coded for *z*–depth. Figure 11(c-f) shows *x*–*y* projections of 2 µm thick slices in which individual mitochondria can be clearly resolved. One major advantage of light-sheet illumination for whole-cell 3D imaging is that there is no photo-bleaching of out-of-focus fluorophores. This is clearly demonstrated by the slower decrease in number of accepted localizations per repeat cycle (single scan through whole-cell) (Fig. 12) for light-sheet compared to wide field illumination. This results in an overall higher number of accepted emitters which contributes to a better image quality and resolution. This is clearly shown in the zoomed in regions of single mitochondria in Fig. 11(c-f) which are much better defined for the light-sheet illuminated cell (Fig. 11(d,f)) than for the wide field illuminated cell (Fig. 11(c,e)).

6. Discussion

For SMSR imaging epi-fluorescence microscopes are the currently the standard. TIRF illumination is often necessary to prevent high background from out-of-focus fluorphores, however this limits the application of SMSR to the ventral membrane of cell. This limitation provided the motivation to develop a simple device that can be used on an epi-fluorescence microscope to improve SMSR imaging by providing light-sheet illumination of the sample.

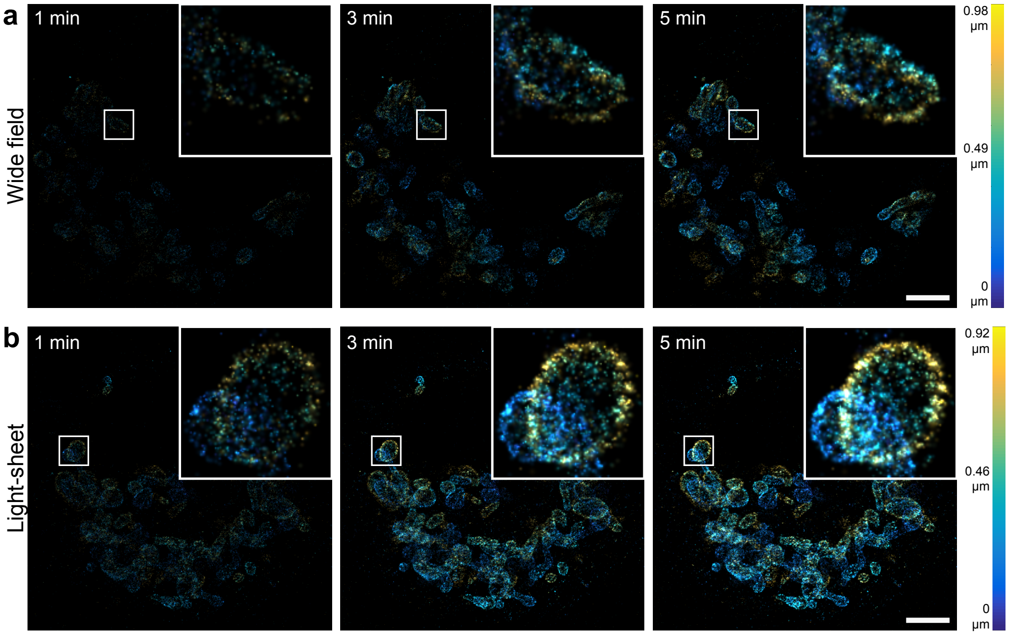

Fig. 10. SO-LSM speeds-up acquisition of 3D super-resolution data. HeLa cells were labeled for TOM-20 to visualize mitochondria and imaged at a single plane for 5 minutes using wide field (a) and light-sheet illumination (b). 3D reconstructions are shown for data acquired in 1, 3 and 5 minutes. Zoom of single mitochondria are shown from the white boxed regions. z–position of emitters is indicated by color coding. Scale bar 2 µm.

To implement SO-LSM on an existing epi-fluorescence microscope a side-port could be used to incorporate a light-sheet generating light-path. The microfluidic chip with 45° mirror surfaces can be packaged in any shape plastic packaging to fit on any microscope stage. For cell and buffer loading regular syringes with or without a syringe pump can be used. This makes SO-LSM a cheap and simple alternative to more complicated and expensive optical systems for whole-cell 3D super-resolution imaging such as structured illumination [24] or lattice light-sheet microscopy [9]. Furthermore SMSR imaging is sped up by the increased laser intensity from the focusing of the light-sheet which overcomes the need to use more powerful and expensive lasers. This benefit also appears in HILO microscopy [11], however the sheet intensity in HILO varies with z–depth within the sample, whereas with SO-LSM the intensity gain is the same at each z–position.

We showed that SO-LSM improves the image quality in diffraction limited imaging. The microfluidic chip with 45° mirror surfaces can therefore also be used for live-cell imaging. Both single plane as well as whole-cell imaging will benefit from light-sheet illumination due to reduced background and decreased photo-bleaching and photo-toxicity. We showed that we can incorporate cells into a gel, which can be perfused on chip. This opens up the possibility to image live cells in a 3D environment created by a gel or matrix with high speed and good image quality.

7. Conclusion

In conclusion, we have shown that a microfluidic chip with incorporated 45° mirror surfaces can be used for light-sheet illumination with a single objective. This system provides decreased

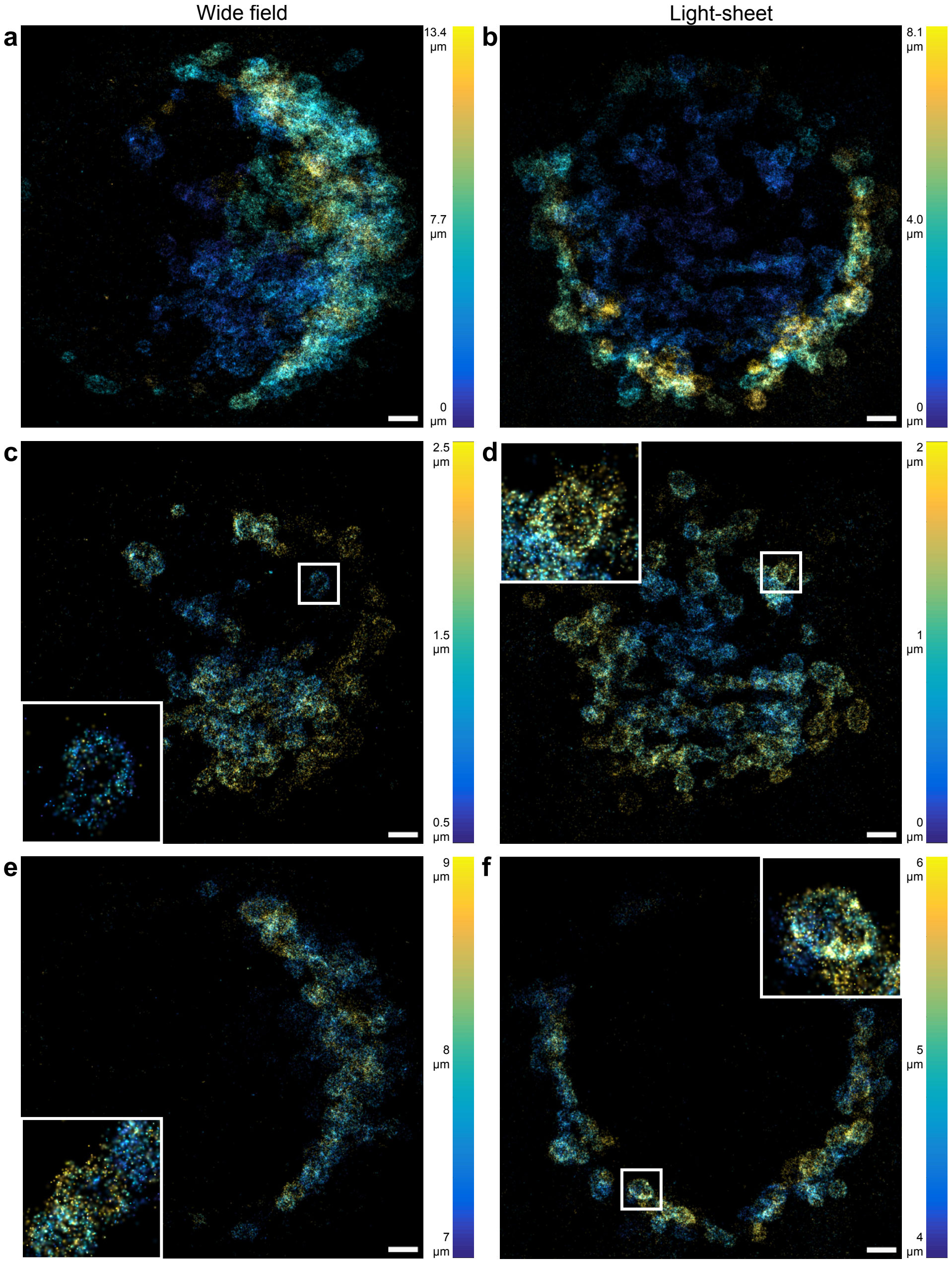
Wide field
Light-sheet
a
13.4 µm
7.7 µm
0 µm
b
8.1 µm
4.0 µm
0 µm
c
2.5 µm
1.5 µm
0.5 µm
d
2 µm
1 µm
0 µm
e
9 µm
8 µm
7 µm
f
6 µm
5 µm
4 µm

Fig. 11. SO-LSM improves whole-cell 3D super-resolution microscopy. HeLa cells were labeled for TOM-20 to visualize mitochondria and imaged using the 3D SMSR method. Cells were imaged from bottom to top and sequences of 2000 frames were acquired at z–planes spaced 250 nm apart. The scan through the cell was repeated 12 times. x–y projections of reconstructed images with color coded z–depth are shown for cells imaged using wide field (a,c,e) and light-sheet illumination (b,d,f). Zoom of single mitochondria are shown from the white boxed regions. Z-position of emitters is indicated by color coding. Image are reconstructed from whole-cell data (a,b) and 2 µm thick slices (c,d,e,f). LS = light-sheet, WF = wide field, scale bars 1 µm

#258956 Received 29 Feb 2016; revised 12 Apr 2016; accepted 9 May 2016; published 17 May 2016

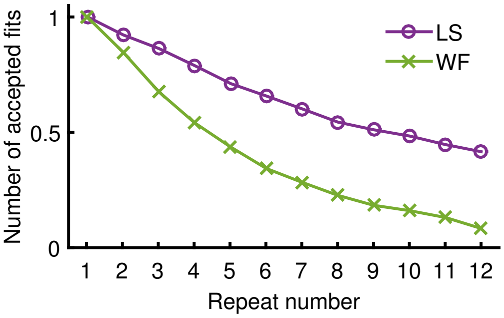

Fig. 12. SO-LSM reduces bleaching during whole-cell 3D super-resolution microscopy. Relative number of accepted fits per repeat (normalized to max) are shown for the data from figure 11. LS = light-sheet, WF = wide field

background in diffraction limited imaging. We demonstrated that using the SO-LSM approach we achieve a large background reduction in SMSR resulting in a higher SNR and a better localization accuracy. Moreover, photobleaching is significantly reduced in 3D whole-cell imaging, resulting in more localizations and improved reconstructed image quality. And due to the increased intensity in the light-sheet we can speed up the acquisition up to 2.5 fold. SO-LSM is easily applicable on any common inverted epi-fluorescence microscope in which a side-port can be used for light-sheet generation. Therefore SO-LSM provides a simple method to greatly improve whole-cell 3D super-resolution microscopy.

Acknowledgments

We would like to thank Mylan Panteah for technical assistance, Shayna Lucero for cell culture assistance, Dr. Mark Olah for help with the data analysis code and Dr. Diane Lidke for helpful advice and critical reading of the manuscript. The research described in this paper was primarily supported by an NIH/NGMS (1R21GM104691) grant awarded to K.A.L. and C.D.J. Additional support was provided by NIH P50GM085273 and by a Rubicon grant from the Netherlands Organization for Scientific Research (NWO Rubicon 825.14.020) awarded to M.B.M.M. Sandia National Laboratories is a multi-program laboratory managed and operated by Sandia Corporation, a wholly owned subsidiary of Lockheed Martin Corporation, for the U.S. Department of Energys National Nuclear Security Administration under Contract DE-AC04-94AL85000.